

Detection of Adversarial Physical Attacks in Time-Series Image Data

Ramneet Kaur*
Computer and Information Science
University of Pennsylvania
Philadelphia, PA, USA
ramneetk@seas.upenn.edu

Yiannis Kantaros*
Electrical and Systems Engineering
Washington University in St. Louis
St. Louis, MO, USA
ioannisk@wustl.edu

Wenwen Si*
Computer and Information Science
University of Pennsylvania
Philadelphia, PA, USA
wenwens@seas.upenn.edu

James Weimer
Computer Science
Vanderbilt University
Nashville, TN, USA
james.weimer@vanderbilt.edu

Insup Lee
Computer and Information Science
University of Pennsylvania
Philadelphia, PA, USA
lee@cis.upenn.edu

Abstract—Deep neural networks (DNN) have become a common sensing modality in autonomous systems as they allow for semantically perceiving the ambient environment given input images. Nevertheless, DNN models have proven to be vulnerable to adversarial digital and physical attacks. To mitigate this issue, several detection frameworks have been proposed to detect whether a *single* input image has been manipulated by adversarial *digital* noise or not. In our prior work, we proposed a real-time detector, called VisionGuard (VG), for adversarial physical attacks against single input images to DNN models. Building upon that work, we propose VisionGuard* (VG*), that couples VG with majority-vote methods, to detect adversarial physical attacks in *time-series image data*, e.g., videos. This is motivated by autonomous systems applications where images are collected over time using onboard sensors for decision making purposes. We emphasize that majority-vote mechanisms are quite common in autonomous system applications (among many other applications), as e.g., in autonomous driving stacks for object detection. In this paper, we investigate, both theoretically and experimentally, how this widely used mechanism can be leveraged to enhance performance of adversarial detectors. We have evaluated VG* on videos of both clean and physically attacked traffic signs generated by a state-of-the-art robust physical attack. We provide extensive comparative experiments against detectors that have been designed originally for out-of-distribution data and digitally attacked images.

Index Terms—adversarial detectors, adversarial examples, neural networks, image classification

I. INTRODUCTION

Deep neural networks (DNN) have seen renewed interest in the last decade due to the vast amount of available data and recent advances in computing. In autonomous systems, DNN are typically used as feedback controllers, motion planners, or perception modules such as object detection and classification. Nevertheless, brittleness of DNN has resulted in unreliable behavior and public failures, e.g., Tesla cars’ crashes and Uber running a red light [1]. In fact, several adversarial attack methods have been proposed recently that aim to minimally

manipulate inputs to DNN models to cause desired incorrect outputs that would benefit an attacker. In image classification, that is also considered in this paper, adversarial attacks are typically categorized as digital and physical ones. The latter augment the physical world by placing adversarial stickers on the surface of objects of interest [2], [3], [4], [5], [6] (see e.g., Fig. 1), while the former embeds an imperceptible amount of digital noise to the classifier input data [7], [8], [9]. Digital attacks typically assume a threat model in which the adversary can feed data directly into the machine learning component. This is not necessarily the case for systems operating in the physical world, such as mobile robots or driverless cars that are using signals from cameras and other sensors as input. Motivated by these applications, this paper focuses exclusively on adversarial physical attacks.

Several *detectors* have been proposed recently to detect adversarially attacked images; see Section I-A. Nevertheless, the large majority of these works primarily focus on determining whether a single image has been manipulated adversarially by a digital attack or not. To the contrary, in this paper, we focus on *detecting* adversarial *physical* attacks against DNN for image classification tasks in *time-series image data* (e.g., videos). Our work is motivated by autonomous driving applications, where a time-ordered sequence of images, collected by onboard cameras, containing objects of interest is available that is used for control purposes. For instance, consider an autonomous car collecting images of a stop sign as it approaches an intersection. Our goal is to determine if the objects (e.g., traffic signs) in the collected images have been manipulated by adversarial targeted physical attacks proposed in [4]; examples of attacked traffic signs using [4] are shown in Fig. 1.

In particular, we consider the following problem. We assume that a time-ordered sequence of images containing a single object of interest is given. We also assume the existence of a perfect object tracking algorithm that is capable of creating an ordered sequence containing the same object. This

*Authors with equal contribution.

assumption can be relaxed by using e.g., recent probabilistic data association algorithms that can associate semantic sensor measurements to objects; see e.g., [10]. Our goal is to determine whether the object captured in the time-series data has been adversarially manipulated [4]. To achieve this, we design a new, simple yet effective, time-series detector, called VisionGuard* (VG*). The proposed time-series detector builds upon (i) VisionGuard (VG), a recently proposed single-image detector against various digital attacks and the physical attacks [11], and (ii) majority vote mechanisms. Specifically, VG* consists of the following two steps: (1) VG is applied to all images that lie within a sliding detection window (capturing how many past images will be used) classifying each image as either adversarial or clean; (2) majority-vote is applied over the VG outputs. If the majority of the VG outputs is ‘adversarial’, then VG* classifies the object under investigation as adversarial; otherwise, it is considered clean. Intuitively, the detection performance of VG* should increase as the size of available data increases or, equivalently, the length of the sliding window increases. To formalize this intuition, we provide conditions about the length of the sliding window and the detection accuracy of VG, under which the time-series detector achieves better detection performance than the single-image detector. In other words, this result shows that, as expected, exploiting past observations of an object interest - instead of relying only on the current input image - can enhance performance of adversarial detectors resulting in safer perception-based control loops. We emphasize that majority-vote mechanisms are quite common in autonomous system applications (among several other applications), as e.g., in autonomous driving stacks [12] for object detection. Our goal is to investigate how this widely used mechanism can be leveraged to enhance performance of adversarial detectors.

We demonstrate the efficiency of VG* on videos of clean and physically attacked traffic signs using stickers designed as in [4]. Additionally, we highlight that VG can be replaced by any other single-image detector to construct a time-series detector. Particularly, in our experiments, we compare the performance of VG* against time-series detectors constructed by simply replacing VG in step (1) with the detectors developed in [13], [14]. We note that [13] proposes a detector for digitally attacked and out-of-distribution (OOD) data, while [14] focuses exclusively on digital attacks. Our experiments validate the previously theoretical connection between the length of detection window and the accuracy of the employed single-image detector, i.e., the more accurate the single-image detector, the better the performance of the corresponding time-series detector as the window length increases. Finally, in the appendix, we provide new comparative experiments of VG against the detectors in [13], [14] on adversarial patches [5] that do not exist in the original paper that proposed VG [11]. The adversarial attack in [5] generates patches that can be placed in the vicinity of an object of interest to cause desired misclassifications. Our comparative experiments further validate the claim made in [11] that existing detectors that have been originally developed for digitally attacked or OOD data, as e.g.,



Fig. 1. Traffic signs manipulated adversarially by the RP_2 attack [4] to fool LISA-CNN. The stickers have been placed so that the stop, yield and speed limit signs are classified as speed limit 35, speed limit 35, and turn right signs, respectively [11].

[13], [14], may perform poorly at detecting physical attacks.

A. Related Work

To protect DNN-based image classifiers from adversarial attacks, several detection and monitoring methods have recently been proposed. Similar to our work, these methods aim to identify whether a given input image has been manipulated or not. As it will be discussed later in the text, unlike our work, the large majority of existing detectors focuses on *single* images that may have been under *digital* attacks. A summary of such works follows. To detect adversarial images, application of image transformation and processing techniques to input images has been proposed in [15], [16], [14], [17], [18]. VG, mentioned earlier, also lies in this category [11]. Adversarial detectors that rely on identifying adversarial subspaces in a manifold of clean data have also been proposed [19], [20], [21], [22], [23], [13]. Related is also the recent work in [24] that uses coverage criteria to detect adversarial inputs. Defenses that rely on training separate DNN that are capable of identifying adversarial images have been proposed as well [25], [26], [27]. Ensembles of previously discussed detectors and defenses against adversarial attacks is considered in [28]. A more comprehensive summary of existing defenses against adversarial inputs can be found in [29], [30]. We emphasize that the above defenses have been evaluated only on digital attacks and on single input images.

OOD detection techniques proposed in [31], [32] have been evaluated against a physical attack [6]. Reconstruction error by variational auto-encoder on a *single input image* relative to the training data is used as the non-conformity measure (NCM) for OOD detection in [31]. [32] propose computing prototypes from the training data and using the distance of an input image from these prototypes for OOD detection on a *single input image*. A similar line of work for OOD detection in time-series data based on NCM has been proposed [33]. This work uses error in equivariance with respect to temporal transformations learned on the in-distribution data as the non-conformity score for detection. They, however, do not consider the detection of adversarial attacks.

Defenses against adversarial patches have also been proposed in [34], [35], [36], [37], where robust training methods have been proposed to enhance the resiliency of the DNN classifier against adversarial inputs. Unlike these, this paper focuses on *detecting* physical attacks without modifying the structure of the DNN image classifier. In fact, detection frameworks are complementary to robust training methods, as the former essentially aim to monitor the input to DNN models (whether

they are trained in a robust fashion or not). Moreover, as discussed earlier, we note that the proposed time-series detector is modular in the sense that VG (step (1)) can be replaced by any other single-image detector such as [6] or [13], [14]. Additionally, we provide the first evaluation of adversarial detectors [13], [14], originally proposed for digital attacks and/or OOD data, against state-of-the-art robust physical attacks [4], [5] and we show that under certain conditions their performance can be improved by exploiting historical data.

B. Contribution

The contributions of this paper can be summarized as follows. *First*, we introduce a new, simple, yet effective and modular, detection framework for physical attacks in time-series image data. *Second*, unlike the large majority of existing detectors that focus on digital attacks or OOD data, this paper focuses on physical attacks and provides the first evaluation of these detectors against physical attacks. *Third*, we show that the proposed framework is computationally efficient allowing for its employment in real-time applications, where images are collected online. *Fourth*, we provide conditions for VG (or any other employed single-image detector) and the length of the sliding detection window (or equivalently the size of historical data) that need to be satisfied so that the time-series detector VG^* performs better than VG (or the corresponding employed single-image detector). *Fifth*, we provide extensive comparative experiments against robust physical attacks demonstrating the efficiency of VG^* .

II. PROBLEM FORMULATION

Consider a classifier $f : \mathcal{X} \rightarrow \mathcal{C}$, where \mathcal{X} is the set of images $x \in \mathbb{R}^m$, where m is the number of pixels, and \mathcal{C} is the set of labels. Let $L(x)$ and $f(x)$ denote the true and the predicted label of image $x \in \mathcal{X}$, respectively. Consider also an attacker that aims to attack f to cause desired misclassifications. In particular, here we consider physical attacks that aim to place adversarial stickers on the surface of objects of interest (e.g., traffic signs) so that an image x that includes a physically attacked object gets a desired (wrong) label $t(x)$ i.e., $f(x) = t(x)$ and $t(x) \neq L(x)$. In section II-A, we review a targeted robust physical attack [4]. In Section II-B, we present the adversarial detection problem that this paper addresses.

A. Robust Physical Perturbations

A targeted robust physical attack is presented in [4] to generate robust visual adversarial perturbations under different physical conditions. The first step requires to solve the following optimization problem that generates adversarial (digital) noise δ : $\min_{\delta} \lambda \|M_x \delta\|_p + NPS + \mathbb{E}_{x_i \sim X^V} J(f(x_i + T_i(M_x \delta)), y^*)$, where (i) M_x is a mask applied to image x to ensure that the perturbation is applied only to the surface of the object of interest (e.g., on a traffic sign and not in the background); (ii) NPS is a non-printability score to account for fabrication error; (iii) X^V refers to a distribution of images containing an object of interest (e.g., a stop sign) under various environmental conditions captured by digital and physical transformations



Fig. 2. Perturbation generated by the RP_2 attack using the authors-provided code under the ℓ_1 norm so that a stop, yield, and speed limit 35 sign are misclassified by the LISA CNN [4] as speed limit 35, speed limit 35, and turn right sign, respectively. These images are used as a guide to place adversarial stickers on the surface of traffic signs as in Fig. 1.

(resulting in attacks being robust to various environmental conditions); (iv) $T_i(\cdot)$ denotes the alignment function that maps transformations on the object to transformations on the perturbation (e.g., if the object is rotated, the perturbation is rotated as well); and (v) y^* is the target label. Finally, an attacker will print out the optimization result on paper, cut out the perturbation M_x , and put it onto the target object. The perturbation generated using the L_1 norm along with its physical application is shown in Figure 2. Observe in this figure, that the L_1 norm generates a sparse attack vector allowing the attacker to physically implement the attack with black/white stickers, as shown in Fig. 1.

B. Detection Problem

Consider an input image x_t , collected at a time instant $t \geq 0$, to the DNN image classifier f which contains a single object of interest. Consider also an ordered sequence $X_{0:t-1} = x_0, x_1, \dots, x_{t-1}$ of images x_n , $n \in \{0, 1, \dots, t-1\}$ containing the same object of interest as x_t does. For instance, consider an autonomous car approaching a stop sign. In this case, x_t is the current input image - containing the stop sign - to the DNN-based perception system f while $X_{0:t-1}$ denotes a time-ordered sequence of observations/images of the same stop sign taken as the car was approaching it. Our goal in this paper is to build a detection method that determines if x_t is an adversarial image, i.e., if x_t contains an object that has been physically attacked, by leveraging the available historical data $X_{0:t-1}$. We note that in this paper we assume the existence of a perfect object tracking algorithm that is capable of creating an ordered sequence $X_{0:t}$ containing the same object. This assumption can be relaxed by using e.g., recent data association algorithms [10], which however, is out of the scope of this paper. The problem that this paper addresses can be summarized as follows:

Problem 1. Given (i) a DNN $f : \mathcal{X} \rightarrow \mathcal{C}$ that is subject to physical attacks discussed in Section II-A; (ii) an input image $x_t \in \mathcal{X}$ under investigation containing an object of interest; and (iii) an ordered sequence of past observations/images $X_{0:t-1}$ containing the same object of interest as x_t does, our goal is to design a detector $f_d : \mathcal{X}_{0:t} \rightarrow \{\text{adversarial, clean}\}$ that classifies the current input image x_t as adversarial or clean given a sequence of past observations $\mathcal{X}_{0:t-1}$.

III. VISIONGUARD*: A NEW ADVERSARIAL TIME-SERIES DETECTOR

To solve Problem 1, we present a time-series detector that builds upon VisionGuard (VG), an existing single-image adversarial detector [11]. To this end, first, in Section III-A, we review VG. Second, in Section III-B, we propose a time-series detector to address Problem 1. Finally, in Section III-C, we demonstrate the effect of using historical data, that exist in time-series data, on detection performance.

A. VisionGuard: A Single-Image Adversarial Detector

VG is a dataset- and attack-agnostic detector that relies on the observation that adversarial inputs are not robust to certain transformations in the sense that these transformations change the output of the DNN significantly [11]. Typically, such transformations are (i) label-invariant, i.e., the true class of the object of interest should not change under this transformation, and (ii) squeeze out features that may be unnecessary for correct classification such as adversarial components. In [11], it was shown that lossy compression and brightness transformations can alleviate the effect of digital and physical attacks, respectively.

VG comprises four steps to detect whether an input image x is adversarial or not. First, the input image x is fed to the classifier f to get the softmax output denoted by $\mathbf{g}(x)$. Second, a user-specified transformation $t : \mathcal{X} \rightarrow \mathcal{X}$ is applied to x to get an image $x' = t(x)$. Third, x' is fed to the classifier to get the softmax output denoted by $\mathbf{g}(x')$. Fourth, x is classified as adversarial if the softmax outputs $\mathbf{g}(x)$ and $\mathbf{g}(x')$ are significantly different. Formally, similarity between $\mathbf{g}(x)$ and $\mathbf{g}(x')$ is measured using the K-L divergence measure, denoted by $D_{\text{KL}}(\mathbf{g}(x), \mathbf{g}(x'))$ and defined as follows: $D_{\text{KL}}(\mathbf{g}(x), \mathbf{g}(x')) = \sum_{c \in \mathcal{C}} \mathbf{g}_c(x) \log \frac{\mathbf{g}_c(x)}{\mathbf{g}_c(x')}$ where $\mathbf{g}_c(x)$ denotes the c -th entry in the softmax output vector $\mathbf{g}(x)$; in other words, $\mathbf{g}_c(x)$ can be viewed as the probability that the class of image x is c . Specifically, if

$$J(x, x') = \min(D_{\text{KL}}(\mathbf{g}(x), \mathbf{g}(x')), D_{\text{KL}}(\mathbf{g}(x'), \mathbf{g}(x))) \quad (1)$$

is greater than a threshold τ , then x is classified as an adversarial input, i.e., $\hat{f}_d(x) = 1$ (i.e., x is adversarial); otherwise, x is classified as a legitimate/clean image, i.e., $\hat{f}_d(x) = \text{clean}$. In [38], it is mentioned that performance of VG can be improved if the max, instead of the min, operator is employed in (1). Hereafter, to stay consistent with [11], we use the min operator. The detection threshold is selected using Receiver Operating Characteristics (ROC) graphs. Given an ROC graph computed on a validation set, a threshold that yields high true positive and low false alarm rate is selected.

B. VisionGuard*: Detecting Attacks in Time-Series Image Data

In what follows, we build a new modular time-series detector, called VisionGuard* (VG*), that classifies an image x_t as clean or adversarial, given a sequence $\mathcal{X}_{0:t-1}$ of past images/observations. As mentioned in Section II-B, hereafter, we assume that all images in the sequence $\mathcal{X}_{0:t}$ contain the same object of interest. Particularly, let $X_{0:t-1} = x_0, x_1, \dots, x_{t-1}$

Algorithm 1 VisionGuard*: Time-Series Detector

Input: {Length T of detection window; Sequence of images $X_{t-T:t}$; Single-Image detector \hat{f}_d }
Output: $\{f_d(x_t|X_{t-T:t-1}) = 1$ if x_t is adversarial, and $f_d(x_t|X_{t-T:t-1}) = 0$ otherwise}
 Feed images x_n to \hat{f}_d for all $n \in \{t-T, t-T+1, \dots, t\}$
 Compute $s(x_t)$ as in (2)
 Initialize $f_d(x_t|X_{t-T:t-1}) = 0$
if $s(x_t) \geq 0.5$ **then**
 $f_d(x_t|X_{t-T:t-1}) = 1$
end if

be an ordered sequence of $t-1$ past observations/images x_n , $n \in \{0, 1, \dots, t-1\}$ and x_t denote the current input image. Also, let $T \geq 0$ denote the length of a sliding detection window capturing how many past images from $X_{0:t}$ can be used. To determine whether x_t is an adversarial image, we examine what is the output of \hat{f}_d on the last T images (including x_t). Then a majority-vote mechanism is employed to reason about x_t ; see Alg. 1. Formally, the proposed detector is constructed as follows. First, we compute the average output of \hat{f}_d over the past T images as follows:¹

$$s(x_t) = \begin{cases} \frac{\sum_{n=t-T}^t \hat{f}_d(x_n)}{T} & \text{if } t \geq T \\ \frac{\sum_{n=0}^t \hat{f}_d(x_n)}{T} & \text{otherwise} \end{cases} \quad (2)$$

Observe that if $s(x_t) \geq 0.5$, then this means that the majority of the past T images, including the current image x_t , are classified as adversarial. Otherwise, the majority is classified as clean. Thus, given $s(x_t)$, we define a time-series detector f_d that complies with majority vote, i.e.,

$$f_d(x_t|X_{t-T:t-1}) = \begin{cases} 1 \text{ (i.e., adversarial)} & \text{if } s(x_t) \geq 0.5 \\ 0 \text{ (i.e., clean)} & \text{otherwise} \end{cases} \quad (3)$$

Remark III.1 (Variants of the Time-Series Detector). *We note that VG* can be extended in various ways. First, any single image detector can be used in place of VG to reason about a single image; see Section IV. Second, to reason about a single image frame x_n , majority-vote over the output of an ensemble of single-image detectors can be applied as opposed to simply relying to the VG output. Alternatively, an ensemble of DNN image classifiers can be used (as opposed to a single one considered in this paper) as in [39]. Once a single image x_n has been classified as adversarial or clean using any of the above ways, majority vote can be applied as in (2)-(3).*

C. Enhancing Detection Performance via Historical Data

In this section, we provide conditions for the single-image detector \hat{f}_d and the length T of the sliding detection window

¹Note that (2) can be written more generally as the weighted average of the detector outputs where e.g., a larger weight is assigned to more important frames. For instance, in an autonomous driving setup, a larger weight to collected images as the car approaches the object of interest (e.g., a traffic sign).

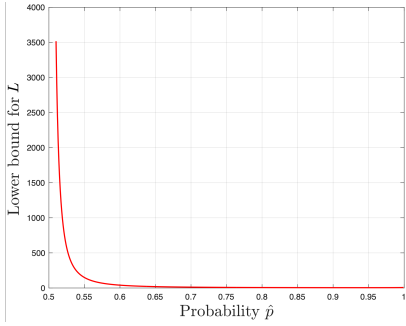


Fig. 3. Graphical illustration of Proposition III.2. The curve corresponds to the lower bound (4). Observe that as $\hat{p} \rightarrow 1$, the lower bound for the length L that needs to be satisfied so that the time series detector f_d performs better than the single-image detector \hat{f}_d decreases. For example, if $\hat{p} = 0.6$ then $L > 40.24$, while if $\hat{p} = 0.9$ then $L > 4.69$.

that need to be satisfied so that the proposed time-series detector f_d achieves better detection performance than \hat{f}_d . These conditions are formally stated in the following proposition; see also Fig. 3.

Proposition III.2. *Let x_t denote an image under investigation and $X_{0:t-1}$ be a time-ordered sequence of images. Assume that x_t and $X_{0:t-1}$ contain the same object of interest. Also let $\hat{f}_d : \mathcal{X} \rightarrow \{0, 1\}$ denote a single-image detector with probability \hat{p} of correct classification/output. Then if (i) the outputs of \hat{f}_d over all images in $X_{0:t-1}$ and x_t are independent; (ii) $\hat{p} > 0.5$; and (iii) the number L of available past images in $X_{0:t-1}$ to reason about x_t satisfies the following condition:²*

$$L > \frac{2[\ln(2) - \ln(1 - \hat{p})]}{(2\hat{p} - 1)^2}, \quad (4)$$

then, it holds that $p > \hat{p}$, where p denotes the probability of correct classification of the time-series detector f_d .

Proof. This result is shown by applying Hoeffding's inequality. Let $X_{t-T:t}$ be the ordered sub-sequence of images that lie within the sliding detection window of f_d . We define random variables Y_n that are 1, if \hat{f}_d classifies the corresponding image x_n correctly, and 0 otherwise, for all $n \in \{t - T, \dots, t\}$. Next, we define $Y_{x_t} = \sum_{n=t-L}^t Y_n$, i.e., Y_{x_t} is a random variable counting the number of correct classifications of \hat{f}_d over the sub-sequence of images $X_{t-L:t} = x_{t-L}, x_{t-L+1}, \dots, x_t$. By definition, Y_{x_t} follows a binomial distribution with mean $T\hat{p}$. By construction of f_d the probability that f_d misclassifies x_t , satisfies: $\mathbb{P}(f_d(x_t) \neq c(x_t)) = 1 - p = \mathbb{P}(Y_{x_t} < \frac{L}{2})$, where $c(x_t)$ denotes the correct 'adversarial' label of x_t , i.e., $c(x_t) \in \{\text{clean, adversarial}\}$. Thus, we have that: $\mathbb{P}(f_d(x_t) \neq c(x_t)) = \mathbb{P}(Y_{x_t} < \frac{L}{2}) \leq \mathbb{P}(Y_{x_t} - L\hat{p} < \frac{L}{2} - L\hat{p}) \leq \mathbb{P}(|Y_{x_t} - L\hat{p}| > \frac{L(2\hat{p}-1)}{2}) = \mathbb{P}(|Y_{x_t} - \mathbb{E}(Y_{x_t})| > \frac{L(2\hat{p}-1)}{2}) \leq 2e^{-\frac{L(2\hat{p}-1)^2}{2}}$ where the last inequality is due to Hoeffding's inequality. Note that Hoeffding's inequality can be applied if (a) Y_n are independent random variables, which holds by assumption (i) and (b) $\frac{L(2\hat{p}-1)}{2} > 0$, which holds since, by assumption (ii), we have $\hat{p} > 0.5$.

²Notice that by construction of f_d , we have that L is defined as follows: $L = \min\{t, T\}$, i.e., $L = T$ if $t \geq T$ and $L = t$ otherwise.

Observe that the derived upper bound (i.e., $2e^{-\frac{L(2\hat{p}-1)^2}{2}}$) goes to 0 as L goes to infinity. Next, using this upper bound, we show that if L satisfies (4) then the detection performance of f_d is greater than the performance of \hat{f}_d , i.e., $p > \hat{p}$ or, equivalently, $1 - p < 1 - \hat{p}$. In math, we show that the following inequality

$$\mathbb{P}(f_d(x_t) \neq c(x_t)) - \mathbb{P}(\hat{f}_d(x_t) \neq c(x_t)) < 0, \quad (5)$$

where $\mathbb{P}(f_d(x_t) \neq c(x_t)) = 1 - \hat{p}$, holds if (4) is true. An over-approximate range of values for L so that (5) is satisfied can be found by using the above derived upper bound. Specifically, in what follows, we compute values for L so that $2e^{-\frac{T(2\hat{p}-1)^2}{2}} - (1 - \hat{p}) < 0$. Solving this inequality for L yields (4).³ Note that this lower bound is positive since $\ln(2) \approx 0.69 > 0$ while $-\ln(1 - \hat{p}) > 0$ due to $1 - \hat{p} < 1$. Consequently, if the outputs of the single image detector \hat{f}_d are independent, $\hat{p} > 0.5$, and L satisfies (4), then $p > \hat{p}$ completing the proof. \square

Remark III.3. *We note that if the single-image detector satisfies the conditions (i)-(iii) of Prop. III.2, then as $L \rightarrow \infty$, the probability of misclassification for the time-series detector goes to 0. Also, note that Prop. III.2, implies that the length T of the sliding window should be designed so that it is larger than the lower bound captured in (4).*

IV. EXPERIMENTS

In this section, we extensively demonstrate the performance of VG^* and compare its performance against baseline detectors [13], [14] summarized in Section IV-A. Particularly, in Sections IV-B, we first discuss how these baseline time-series detectors are set up. In Section IV-C, we present the data collection process that involves recording videos of clean and adversarial traffic signs. Then, in Sections IV-D- IV-E, we compare the performance of VG^* on the above-mentioned videos against the baseline time-series detectors. Our experiments validate that historical data can enhance performance of single-image detectors, as shown in Proposition III.2. In summary, our comparative experiments show that the proposed detector is characterized by a more consistent performance than the competitive detectors whose performance changes significantly across attacks, datasets, and DNN models. Finally, we discuss the real-time performance of the proposed detectors. All experiments have been executed on a computer with Intel(R) Xeon(R) Gold 6148 CPU, 2.40GHz.

A. Summary of Considered Baseline Detectors

Mahalanobis-based Detector (MD): This detector relies on computing a confidence score for each test sample; if this confidence score is above a threshold then the test image is considered abnormal or out-of-distribution [13]. To define this confidence score, the Mahalanobis distance to the training data set is computed. Specifically, $|\mathcal{C}|$ class-conditional distributions

³Note that this requires to assume that $1 - \hat{p} > 0$, i.e., $\hat{p} < 1$ so that $\ln(1 - \hat{p})$ is well defined. Nevertheless, if $\hat{p} = 1$, then it trivially holds that any length $L \geq 0$ can be used to maintain the perfect performance of the single-image detector.

are defined for each layer of the targeted DNN that are assumed to be Gaussian distributions. In math, for each layer ℓ of the DNN f , the empirical class mean $\mu_{c,\ell}$ and covariance Σ_ℓ of training samples $\{(x_i, y_i)\}_{i=1}^N$, where y_i is the true label of x_i , are defined as follows: (i) $\mu_{c,\ell} = \frac{1}{N_c} \sum_{i:y_i=c} f_\ell(x_i)$; and $\Sigma_\ell = \frac{1}{N_c} \sum_{c \in \mathcal{C}} \sum_{i:y_i=c} (f_\ell(x_i) - \mu_{c,\ell})(f_\ell(x_i) - \mu_{c,\ell})^T$, where N_c is the total number of training samples with label c and $f_\ell(x_i)$ refers to the output of the ℓ -th layer of the DNN f . Then, given a new sample x , for each layer ℓ , the following steps are executed. First, the closest class \hat{c} is computed as per the Mahalanobis distance: $\hat{c} = \operatorname{argmin}_c (f_\ell(x) - \hat{\mu}_{c,\ell})^T \hat{\Sigma}_\ell^{-1} (f_\ell(x) - \hat{\mu}_{c,\ell})$. Second, a small noise is added to x , i.e., $\hat{x} = x - \epsilon \nabla_x (f_\ell(x) - \hat{\mu}_{\hat{c},\ell})^T \hat{\Sigma}_\ell^{-1} (f_\ell(x) - \hat{\mu}_{\hat{c},\ell})$. Third, a confidence score M_ℓ is computed as: $M_\ell = \max_c - (f_\ell(\hat{x}) - \hat{\mu}_{c,\ell})^T \hat{\Sigma}_\ell^{-1} (f_\ell(\hat{x}) - \hat{\mu}_{c,\ell})$. Once these steps are repeated for all layers ℓ , the following confidence score is computed which is used for detection: $M = \sum_\ell \alpha_\ell M_\ell$. This detector has been tested against digital attacks and OOD data [13].

Entropy-based Detector (ED): This detector relies on the observation that digital attacks embed an imperceptible amount of noise to images [14]. Motivated by this observation, the adversarial perturbation is treated as artificial noise and leverages adaptive noise reduction techniques to reduce its adversarial effect, where aggressiveness of the denoising strategy is selected based on the entropy of the image. In particular, this detector comprises the following steps. First, the entropy of an image x with dimensions $M \times N$ is computed as: $H = - \sum_{i=0}^{255} p_i \log_2 p_i$, where $p_i = f_i / (M \times N)$ and f_i is the frequency of pixel level $i \in [0, 1, \dots, 255]$. For RGB images, the entropy is computed as the average of entropies over the three channels. Next, the denoising process follows. First, the image gets quantized using a scalar quantization method where all inputs (i.e., pixel values) within a specified interval are mapped to a common value (called codeword), and the inputs in a different interval will be mapped to a different codeword. The number of intervals for uniform quantization is determined using the entropy of the image. Next, the entropy of the quantized sample is computed to determine if spatial smoothing will be applied. Only if the entropy is larger than a threshold, spatial smoothing (e.g., using a box filter) is applied. The image generated by this adaptive denoising process is denoted by $T(x)$. Finally, the original image x and the filtered one $T(x)$ are sent to the target classifier. If the predicted labels for x and $T(x)$ are the same, then x is considered benign/clean. Otherwise, it is identified as adversarial.

Time-Series Detectors MD* & ED*: Following the same logic as in Section III-B, we construct the time series detectors MD*, and ED* based on the single-image detectors MD, and ED. Specifically, these detectors are built exactly as VG*; the only difference is that VG has been replaced by MD and ED.

B. Setting Up Time-Series Detectors

In what follows, we present the target DNN models and we discuss how we set up the single image detectors, discussed above, for the RP₂ attack on traffic signs. We have selected AdvNet as a training set to configure all detectors; AdvNet is

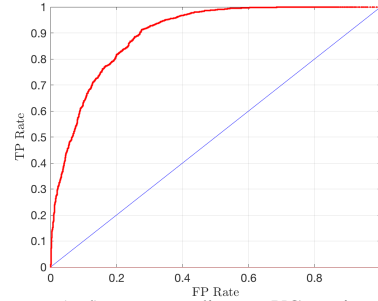


Fig. 4. ROC curve (red) corresponding to VG equipped with brightness transformation with HSV = 200 on AdvNet for LISA CNN [4]. The detection threshold $\tau = 0.43$ yields TP rate = 80% and FP rate = 19% on AdvNet. Each point in the ROC curve corresponds to a detection threshold while the blue line represents the ROC of a random detector.

a recently proposed dataset with clean and physically attacked traffic signs [11]. All detectors are evaluated on a test set constructed by extracting frames of videos with clean and physically attacked traffic signs. More details follow.

Target DNN Models: Hereafter, in our evaluation, we consider the LISA-CNN [4] and the GTSRB-CNN [40] that can classify traffic signs. Both CNNs take as input 32×32 RGB images while LISA and GTSRB CNN have 17 and 43 labels/outputs, respectively. LISA-CNN has 91% accuracy on the LISA test set and the GTSRB-CNN achieves 95.7% accuracy on the GTSRB test set.

VG: As discussed in Section III, to select a detection threshold τ for VG, we construct the ROC curve of VG on AdvNet, which captures the trade-off between the true positive (TP) and false positive/alarm (FP) rate for a range of thresholds. Then, based on the ROC curve, we select a threshold that yields a high TP rate and low FP rate. For instance, the ROC curve when the target neural network is the LISA CNN is shown in Figure 4; the area under this ROC (AUROC) is 89.43%. Then, we pick a threshold $\tau = 0.43$ which yields a TP rate equal to 80% and a FP rate equal to 19%. Following the same process, we select $\tau = 0.78$ for the GTSRB CNN. Note that for both CNNs, VG applies brightness transformation with HSV = 200.

MD: To train the Mahalanobis detector, we followed the same process as we did for VG. First, we compute the ROC of this detector using AdvNet. Then, using the ROC curve, we pick a threshold that yields a high TP and a low FP rate. The AUROC of MD for the LISA CNN is 81.2% which is smaller than the AUROC of VG. In fact, given any fixed TP rate, the corresponding FP rate of MD is higher than that of VG. For instance, for TP rate = 80%, MD yields a FP rate that is approximately 45% (while for VG, TP rate = 19%). Thus, prioritizing a low FP rate, we select a threshold which yields TP rate = 50% and FP rate = 8%. Nevertheless, the choice of the threshold is user- and scenario- specific.

ED: This detector requires the selection of a spatial smoothing filter [14]. In [14], it was shown that 5×5 cross, 7×7 cross, 5×5 diamond, 7×7 diamond, and 5×5 box filters yield satisfactory performance against digital attacks. To pick a filter for physical attacks, we evaluated this detector on AdvNet for various cross, box and diamond filters. The best performance was attained using a 3×3 box filter.



Fig. 5. Snapshots of a recorded video containing a clean stop sign.

C. Data Collection & Evaluation Metric

To evaluate the detection performance of VG^* against the baseline detectors MD^* and ED^* , we have recorded videos of clean and physically attacked stop, yield, and speed limit 35 signs. The traffic signs have been attacked in the same way as in AdvNet. The videos have an average duration of 12 seconds and they were taken during daytime by a 12MP smartphone camera at 30 frames-per-second. Each video contains a single (clean or attacked) traffic sign. At the beginning of the videos, the distance between the camera and the traffic sign is on average 15m which gradually decreases. Snapshots from a representative video are provided in Fig. 5. To compare the detectors, we extract the frames from each video (to construct the time-series data $\mathcal{X}_{0:t}$) and we report the accuracy of each detector defined as follows:

$$\text{Acc}(T) = \frac{\text{number of correctly labeled images } x_t}{\text{total number of images}}, \quad (6)$$

where the images x_t are labeled as ‘clean’ or ‘adversarial’ using the past T frames in the video.

D. Comparative Evaluation on LISA CNN

We evaluate the performance of the time-series detectors VG^* , MD^* , and ED^* on the recorded videos mentioned in Section IV-C. We use these time-series detectors to classify each frame x_t as clean or adversarial. Note that there can be frames without the traffic sign. Thus, the detector uses the past T frames that contained the sign. To reason about whether a traffic sign exists within a frame or not, we train a YOLO v3 object detector - using clean images from AdvNet - that can detect stop, yield and speed limit 35 signs. All detectors have been evaluated on the same videos. The results are summarized in Tables I-VI for LISA CNN. Particularly, we report the accuracy of classifying correctly, as adversarial or clean, the frames on each video for $T \in \{0, 3, 10, T_{\text{all}}\}$ as per (6). Notice that when $T = 0$, the time-series detector coincides with the corresponding single-image detector. The accuracy reported on $T = 0$ can also be viewed as an approximation of the accuracy, denoted by \hat{p} in Proposition III.2, of the single-image detector computed using the frames of the corresponding video. Also, by $T = T_{\text{all}}$, we refer to the case where T is large enough so that the time-series detector considers all past frames in $\mathcal{X}_{0:t-1}$ of the video to reason about x_t , for all $t \geq 0$.

VG^* : In Tables I-II, we show the average detection performance of VG^* across five videos of clean traffic signs considering the LISA CNN. We observed that, in general, if the accuracy of the single-image detector \hat{f}_d on each frame

TABLE I
 VG^* : LISA CNN AND CLEAN TRAFFIC SIGNS

	T=0	T=3	T=10	T=30	T_{all}	DNN Acc
Stop	87.4%	89%	88.6%	90.4%	93%	93.8%
Speed35	85.4%	87.2%	87.4%	95.8%	98.6%	93.8%
Yield	92.6%	95%	97%	100%	100%	99.2%

TABLE II
 VG^* : LISA CNN AND ADVERSARIAL TRAFFIC SIGNS

	T=0	T=3	T=10	T=30	T_{all}	DNN Acc
Stop	97.3%	98.8%	99.8%	99.8%	99.8%	1.6%
Speed35	95.8%	96.6%	97.2%	97.8%	97.8%	0.5%
Yield	86.3%	88.5%	89.8%	90.2%	83.3%	22.3%

is reasonably high (implying that $\hat{p} > 0.5$ as estimated by the $T = 0$ columns), then when T is very large, the time-series detector f_d achieves high performance on distinguishing clean (Table I) and adversarial (Table II) traffic signs. This is also implied by Proposition III.2.

MD^* : The average performance of MD^* across five videos for LISA CNN is summarized in Tables III-IV. Observe that this detector performs quite well on distinguishing clean and adversarial stop and speed limit signs but it performs poorly on yield signs. A potential reason for this is that MD assumes that class-conditions distributions are Gaussian distributions across all layers of the target neural network. This assumption was validated for digitally attacked and OOD data in [13]. Nevertheless, it may not hold for certain physical attacks, as the one considered here. Notice that as T increases, the performance of MD^* does not increase for the yield sign. However, this does not contradict Proposition III.2 as the reported accuracy may be inaccurate (as only a few tens of image frames are used). Recall also that Proposition III.2 does not imply that the detection performance should monotonically increase as T increases. Overall, using the whole image sequence/video, the time-series detector classifies the yield sign (on average across all videos) as clean. In total, the detection performance of MD^* and VG^* is comparable on stop signs but VG^* outperforms MD^* on speed limit/yield signs.

ED^* : The average performance of ED^* across five videos for LISA CNN is summarized in Tables V-VI. Similar to MD^* , observe that the single-image detector ($T = 0$) performs much worse than VG in several videos. The reason is because ED is built using filters aiming to remove digital noise as opposed to e.g., VG that uses brightness transformations to deal with adversarial stickers. As a result, the performance of this detector is satisfactory on clean traffic signs (see Table V) but not on physically attacked traffic signs (see Table VI). Overall, this detector seems to perform quite well on distinguishing clean and adversarial stop signs but it fails to generalize to speed limit and yield signs.

Summary of comparative detection performance: The comparative performance of the resulting time-series detector for the LISA CNN is summarized in Figure 7. Specifically, Figure 7(a) and 7(b) illustrate the average performance of the three time-series detectors across all clean and adversarial traffic signs, respectively, for $T \in \{0, 3, 10, T_{\text{all}}\}$. Observe that the VG -based time-series detector achieves the best performance

TABLE III
MD*: LISA CNN AND CLEAN TRAFFIC SIGNS

	T=0	T=3	T=10	T=30	T_{all}	DNN Acc
Stop	97.4%	99.4%	99.6%	99.8%	99.8%	93.8%
Speed35	72%	80.4%	84.2%	93.8%	99.2%	93.8%
Yield	61.8%	82.4%	51.8%	54.6%	60%	99.2

TABLE IV
MD*: LISA CNN AND ADVERSARIAL TRAFFIC SIGNS

	T=0	T=3	T=10	T=30	T_{all}	DNN Acc
Stop	83.7%	89%	95.2%	95.2%	98.3%	1.6%
Speed35	82.2%	89.2%	95.8%	98.4%	99.2%	0.5%
Yield	34%	33%	33.4%	33.3%	33.3%	22.3%

on average, since it has been designed to be effective against physical attacks as opposed to [13], [14] that focus on digital attacks and/or OOD data. Also, notice that among all considered single-image detectors (i.e., $T = 0$), VG attains the best performance in terms of both the accuracy metric defined in (6) and the AUROC; see Section IV-B.

E. Comparative Evaluation on GTSRB CNN

Next, we compare the performance of VG* against the time-series detectors MD* and ED*, when the GTSRB-CNN is considered. The GTSRB-CNN is trained on the German Traffic Sign Recognition Benchmark. Since we did not have access to German traffic signs for our physical experiments, GTSRB-CNN is evaluated only on videos with US stop signs. The AUROC of VG (with brightness transformation and HSV = 200) and MD for GTSRB-CNN on the AdvNet dataset is 97.81% and 79.9%, respectively. To set up the time series detectors, based on these ROCs, we select thresholds for VG and MD that yield TP rate = 95%, FP rate = 4% and TP rate = 50%, FP rate = 8%. ED* is set up using a 3×3 box filter (exactly as in Section IV-B. The comparative performance of the time-series detectors VG*, MD*, and ED* when the GTSRB-CNN is employed is summarized in Tables VII-IX. As in Section IV-D, these tables report the accuracy, as defined in 6, of the considered time-series detectors for videos containing a clean or adversarial stop sign. The stickers were placed so that the GTSRB-CNN classifies stop signs as speed limit 35 signs as in [11], [4]. Figure 8 visualizes the average performance of VG*, MD*, and ED* across all clean and adversarial videos reported in Tables VII-IX. Observe first that ED* achieves the best (average) performance in distinguishing clean and adversarial stop signs when the GTSRB-CNN is considered. In fact, ED* achieved a satisfactory performance on stop signs when the LISA-CNN was considered but it failed to generalize to other traffic signs (see Section IV-D). VG* performs comparably to ED* for the GTSRB-CNN but it outperforms it when the LISA CNN is considered. MD* achieved the worst performance in the GTSRB-CNN setup. Overall, we observe that VG* achieves a more consistent and satisfactory detection performance as the DNN model and the dataset change.

F. Real-Time Computational Requirements

In this section, we evaluate the real-time computational requirements of the three single-image detectors employed

TABLE V
ED*: LISA CNN AND CLEAN TRAFFIC SIGNS

	T=0	T=3	T=10	T=30	T_{all}	DNN Acc
Stop	86.8%	90.8%	91.2%	93.8%	93.8%	93.8%
Speed35	48.2%	47%	44.2%	44.6%	40.4%	93.8%
Yield	95.8%	98.6%	99.2%	99.6%	99.6%	99.2%

TABLE VI
ED*: LISA CNN AND ADVERSARIAL TRAFFIC SIGNS

	T=0	T=3	T=10	T=30	T_{all}	DNN Acc
Stop	92.7%	94.7%	97.5%	99.7%	100%	1.6%
Speed35	34%	31%	33%	26.6%	11.2%	0.5%
Yield	68.5%	70%	73.8	72.7	77.2	22.3%

above and the resulting time-series detector in terms of required disk-space and execution time. MD requires storing the empirical class mean and covariance for each layer of the DNN that are used at runtime to detect adversarial inputs. Storing this information required 4.4 MB. In contrast, VG and ED do not have any disk-space requirements, as they do not rely on storing information from the training sets. Instead, they apply image transformations and filtering methods in memory. Also, VG, MD and ED require 0.018, 0.023 and 0.049 secs, on average, to check if a single image is adversarial. Note that these runtimes are implementation specific and they may depend on the image dimensions. For instance, VG can be optimized by computing the softmax output of the original and the transformed image in parallel. The employed single-image detectors are fast enough for real time applications, such as autonomous cars. For instance, the YOLO neural network [41] typically operates in autonomous driving applications at 55 frames per second (FPS) (or at 155 FPS for a small accuracy trade off) i.e., 55 images are generated per second [42]. Thus, if the car camera operates at 55 FPS, then a new frame/image is generated every 0.018 seconds. In other words, VG can be used to reason about trustworthiness of each frame while the entropy detector can be used every $0.049/0.018 = 2.78$ frames. Finally, applying majority vote is quite inexpensive. For instance, majority vote required on average 7.1×10^{-6} secs, 8.1×10^{-6} secs, 7.9×10^{-6} secs, and 1.1×10^{-5} secs for $T = 3, 10, 30$ and $T = T_{all}$, respectively. We note that these runtimes ignore any computational burden incurred by e.g., object tracking algorithms that will generate sequences of images containing the same object of interest.

V. CONCLUSION

This paper proposed an effective and modular defense against physical adversarial attacks in time series image data. We provided conditions under which by using historical data, the time series detector performs better than the corresponding single image detector. Finally, we provided extensive experiments to validate the proposed time-series detector.

APPENDIX

In what follows, we compare the performance of the detectors VG, MD, and ED against an adversarial patch [5].

Adversarial Patch: A targeted adversarial patch is presented in [5]. Particularly, to fool a DNN classifier, a part of the image is completely replaced with an adversarial patch. This patch is generated as follows. Given an image x , a patch p that may have



Fig. 6. Examples of ImageNet images attacked by [5] for the target label $y^* = \text{toaster}$.

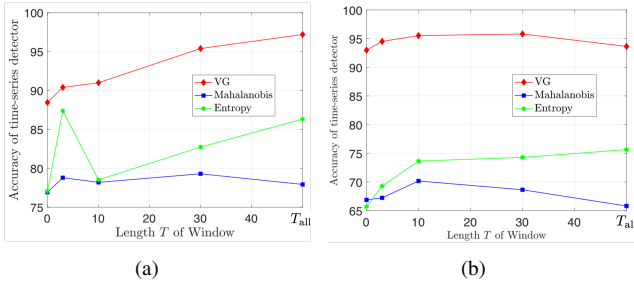


Fig. 7. Comparison of the constructed time-series detectors against clean (Fig. 7(a)) and adversarial traffic signs (Fig. 7(b)) for the LISA CNN.

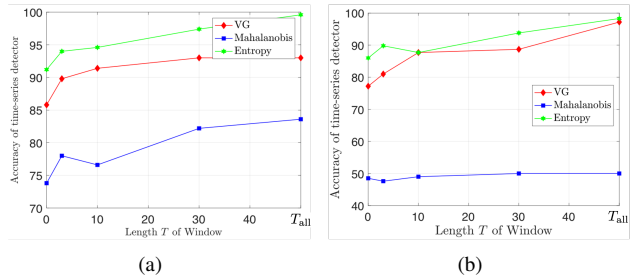


Fig. 8. Comparison of the constructed time-series detectors against clean (Fig. 8(a)) and adversarial stop signs (Fig. 8(b)) for the GTSRB CNN.

any shape, patch location l , and patch transformations t (e.g. rotations or scaling) a patch application operator $A(p, x, l, t)$ is defined which first applies the transformations t to the patch p , and then applies the transformed patch to the image x at location l . The trained patch \hat{p} is trained to optimize the objective function: $\hat{p} = \mathbf{E}_{x \sim \mathcal{X}, t \sim T, l \sim L} \log P(f(A(p, x, l, t)) = y^*)$, where \mathcal{X} is a training set of images, T is a distribution over transformations of the patch, L is a distribution over locations in the image, and $P(f(A(p, x, l, t)) = \hat{y})$ denotes the probability that the classifier will assign to the adversarially patched image $A(p, x, l, t)$ the target label y^* . Note that the expectation is over images as well, which encourages the trained patch to work regardless of what is in the background. The trained patch \hat{p} is obtained in [5] by using a variant of the Expectation over Transformation (EOT) framework presented in [43]. As shown in [5], this attack is effective by either physically placing the sticker in the vicinity of an object of interest or digitally embedding the sticker in the background of given images (see Fig. 6).

Dataset: All detectors are evaluated on the ImageNet (ILSVRC2012) dataset. ImageNet contains 1.4 million RGB 224×224 images divided in 1.2 million training images, 50,000 validation images, 150,000 testing images, with 1000 classes. The adversarial patch is trained as in [5] to fool ResNet 50 with

TABLE VII
VG*: GTSRB CNN - (CLEAN & ADVERSARIAL) STOP SIGNS

	T=0	T=3	T=10	T=30	T_{all}	DNN Acc
Clean Stop	85.8%	89.8%	91.4%	93%	93%	82.8%
Adv Stop	77.2%	81%	87.7%	88.7%	97.2%	13.9%

TABLE VIII
MD*: GTSRB CNN - (CLEAN & ADVERSARIAL) STOP SIGNS

	T=0	T=3	T=10	T=30	T_{all}	DNN Acc
Clean Stop	73.8%	78%	76.6%	82.2%	83.6%	82.8%
Adv. Stop	48.5%	47.6%	49%	50%	50%	13.9%

desired label $y^* = \text{toaster}$. Once the patch is generated, we insert it on a random location on a random ImageNet image. Some examples of adversarially attacked ImageNet images are shown in Figure 6. In our evaluation, we have used the ResNet-50 with 73.6% accuracy on the ImageNet dataset [44].

Evaluation: To compare the performance of the detectors, we compute their corresponding ROC. VG equipped with brightness with HSV values equal to 90 and 200 yields AUROC being equal to 90.2% and 93.5%, respectively; see Fig. 9(a). For example, when $HSV = 160$ a threshold $\tau = 3.6$ yields a TP rate equal to 90% and a FP rate equal to 14.8%. The AUROC of MD is 84.5% which is lower than that of VG; see Fig. 9(b). In fact, by comparing the corresponding ROC curves, we observe that for a given FP rate, VG achieves a higher TP rate. For example, a threshold $\tau = -0.94$ yields a TP rate equal to 80% and a FP rate equal to 24.9%. As in Section IV-D, to configure ED we investigate various spatial filters. The best performance was attained using a 9×9 box mean filter. In this case, ED yields TP and FP rates that are 97% and 32.5%, respectively. Notice that although the TP rate is quite high, the corresponding FP rate may be quite high for certain safety critical applications (e.g., autonomous driving). Overall, VG seems to have a more consistent and ‘robust’ performance across both physical attacks considered in the paper and various models and datasets than MD and ED. We note that VG with brightness transformation and $HSV = 200$ attains a high AUROC under the adversarial patch for various DNN models. For instance, for the DNN models inception v3, vgg16, vgg19 the AUROC is 84.92%, 96.35%, and 95.93%.

REFERENCES

- [1] Verge Staff, “Uber’s fatal self-driving crash: all the news and updates,” *The Verge*, 2018. [Online]. Available: <http://www.theverge.com/2018/3/28/17174636/uber-self-driving-crash-fatal-arizona-update>
- [2] D. Karmon, D. Zoran, and Y. Goldberg, “Lavan: Localized and visible adversarial noise,” *arXiv preprint arXiv:1801.02608*, 2018.
- [3] J. Li, F. Schmidt, and Z. Kolter, “Adversarial camera stickers: A physical camera-based attack on deep learning systems,” in *International Conference on Machine Learning*. PMLR, 2019, pp. 3896–3904.
- [4] K. Eykholt, I. Evtimov, E. Fernandes, B. Li, A. Rahmati, C. Xiao, A. Prakash, T. Kohno, and D. Song, “Robust physical-world attacks on deep learning visual classification,” in *Proceedings of the IEEE Conference on Computer Vision and Pattern Recognition*, 2018, pp. 1625–1634.
- [5] T. B. Brown, D. Mané, A. Roy, M. Abadi, and J. Gilmer, “Adversarial patch,” *arXiv preprint arXiv:1712.09665*, 2017.
- [6] A. Bolor, K. Garimella, X. He, C. Gill, Y. Vorobeychik, and X. Zhang, “Attacking vision-based perception in end-to-end autonomous driving models,” *Journal of Systems Architecture*, vol. 110, p. 101766, 2020.

TABLE IX
ED*: GTSRB CNN - (CLEAN & ADVERSARIAL) STOP SIGNS

	T=0	T=3	T=10	T=30	T _{all}	DNN Acc
Clean Stop	91.2%	94%	94.6%	97.4%	99.6%	82.8%
Adv. Stop	86%	89.8%	87.7%	93.8%	98.3%	13.9%

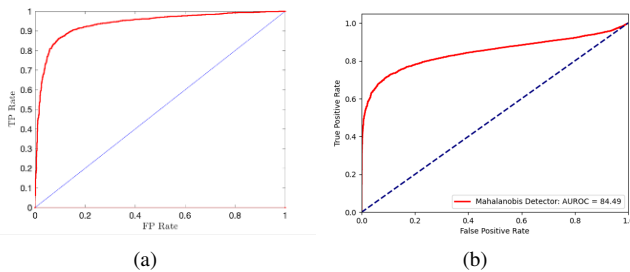


Fig. 9. ROC curve (red) corresponding to VG with brightness transformation and HSV = 200 (Fig. 9(a)) and MD (Fig. 9(b)) on ImageNet and ResNet50 under the adversarial patch [5].

- [7] N. Carlini and D. Wagner, "Adversarial examples are not easily detected: Bypassing ten detection methods," in *Proceedings of the 10th ACM Workshop on Artificial Intelligence and Security*. ACM, 2017, pp. 3–14.
- [8] N. Papernot, P. McDaniel, S. Jha, M. Fredrikson, Z. B. Celik, and A. Swami, "The limitations of deep learning in adversarial settings," in *2016 IEEE European Symposium on Security and Privacy (EuroS&P)*. IEEE, 2016, pp. 372–387.
- [9] S.-H. Choi, J.-M. Shin, P. Liu, and Y.-H. Choi, "Argan: Adversarially robust generative adversarial networks for deep neural networks against adversarial examples," *IEEE Access*, vol. 10, pp. 33 602–33 615, 2022.
- [10] S. L. Bowman, N. Atanasov, K. Daniilidis, and G. J. Pappas, "Probabilistic data association for semantic slam," in *2017 IEEE international conference on robotics and automation (ICRA)*, 2017, pp. 1722–1729.
- [11] Y. Kantaros, T. Carpenter, K. Sridhar, Y. Yang, I. Lee, and J. Weimer, "Real-time detectors for digital and physical adversarial inputs to perception systems," in *Proceedings of the ACM/IEEE 12th International Conference on Cyber-Physical Systems*, 2021, pp. 67–76.
- [12] "Apollo's github page," <https://github.com/ApolloAuto/apollo>, accessed: 2022-06-24.
- [13] K. Lee, K. Lee, H. Lee, and J. Shin, "A simple unified framework for detecting out-of-distribution samples and adversarial attacks," *Advances in neural information processing systems*, vol. 31, 2018.
- [14] B. Liang, H. Li, M. Su, X. Li, W. Shi, and X. Wang, "Detecting adversarial image examples in deep neural networks with adaptive noise reduction," *IEEE Transactions on Dependable and Secure Computing*, 2018.
- [15] S. Tian, G. Yang, and Y. Cai, "Detecting adversarial examples through image transformation," in *Thirty-Second AAAI Conference on Artificial Intelligence*, 2018.
- [16] D. Meng and H. Chen, "Magnet: a two-pronged defense against adversarial examples," in *Proceedings of the 2017 ACM SIGSAC Conference on Computer and Communications Security*. ACM, 2017, pp. 135–147.
- [17] H. Liu, B. Zhao, M. Ji, Y. Peng, J. Guo, and P. Liu, "Feature-filter: Detecting adversarial examples by filtering out recessive features," *Applied Soft Computing*, p. 109027, 2022.
- [18] R. Kaur, S. Jha, A. Roy, S. Park, E. Dobriban, O. Sokolsky, and I. Lee, "iDECODE: In-distribution equivariance for conformal out-of-distribution detection," in *Proceedings of the AAAI Conference on Artificial Intelligence*, vol. 36, no. 7, 2022, pp. 7104–7114.
- [19] R. Feinman, R. R. Curtin, S. Shintre, and A. B. Gardner, "Detecting adversarial samples from artifacts," *arXiv preprint arXiv:1703.00410*, 2017.
- [20] S. Jha, U. Jang, S. Jha, and B. Jalaian, "Detecting adversarial examples using data manifolds," in *IEEE Military Communications Conference (MILCOM)*, Norfolk, VA, 2018, pp. 547–552.
- [21] F. Crecchi, D. Bacciu, and B. Biggio, "Detecting adversarial examples through nonlinear dimensionality reduction," *arXiv preprint arXiv:1904.13094*, 2019.
- [22] T. Pang, C. Du, Y. Dong, and J. Zhu, "Towards robust detection of adversarial examples," in *Advances in Neural Information Processing Systems*, 2018, pp. 4584–4594.
- [23] X. Ma, B. Li, Y. Wang, S. M. Erfani, S. Wijewickrema, G. Schoenebeck, D. Song, M. E. Houle, and J. Bailey, "Characterizing adversarial subspaces using local intrinsic dimensionality," *arXiv preprint arXiv:1801.02613*, 2018.
- [24] G. Rossolini, A. Biondi, and G. Buttazzo, "Increasing the confidence of deep neural networks by coverage analysis," *IEEE Transactions on Software Engineering*, 2022.
- [25] G. Fidel, R. Bitton, and A. Shabtai, "When explainability meets adversarial learning: Detecting adversarial examples using shap signatures," in *2020 International Joint Conference on Neural Networks (IJCNN)*. IEEE, 2020, pp. 1–8.
- [26] G. Cohen, G. Sapiro, and R. Giryes, "Detecting adversarial samples using influence functions and nearest neighbors," in *Proceedings of the IEEE/CVF Conference on Computer Vision and Pattern Recognition*, 2020, pp. 14 453–14 462.
- [27] H. Liu, B. Zhao, Y. Peng, W. Li, and P. Liu, "Towards understanding and harnessing the effect of image transformation in adversarial detection," *arXiv preprint arXiv:2201.01080*, 2022.
- [28] W. He, J. Wei, X. Chen, N. Carlini, and D. Song, "Adversarial example defense: Ensembles of weak defenses are not strong," in *11th {USENIX} workshop on offensive technologies ({WOOT} 17)*, 2017.
- [29] Y. Deng, T. Zhang, G. Lou, X. Zheng, J. Jin, and Q.-L. Han, "Deep learning-based autonomous driving systems: A survey of attacks and defenses," *IEEE Transactions on Industrial Informatics*, 2021.
- [30] S. Bulusu, B. Kailkhura, B. Li, P. K. Varshney, and D. Song, "Anomalous example detection in deep learning: A survey," *IEEE Access*, vol. 8, pp. 132 330–132 347, 2020.
- [31] F. Cai and X. Koutsoukos, "Real-time out-of-distribution detection in learning-enabled cyber-physical systems," in *2020 ACM/IEEE 11th International Conference on Cyber-Physical Systems (ICCPs)*. IEEE, 2020, pp. 174–183.
- [32] Y. Yang, R. Kaur, S. Dutta, and I. Lee, "Interpretable detection of distribution shifts in learning enabled cyber-physical systems," in *2022 ACM/IEEE 13th International Conference on Cyber-Physical Systems (ICCPs)*. IEEE, 2022, pp. 225–235.
- [33] R. Kaur, K. Sridhar, S. Park, S. Jha, A. Roy, O. Sokolsky, and I. Lee, "CODiT: Conformal out-of-distribution detection in time-series data," *arXiv preprint arXiv:2207.11769*, 2022.
- [34] P.-y. Chiang, R. Ni, A. Abdelkader, C. Zhu, C. Studer, and T. Goldstein, "Certified defenses for adversarial patches," *arXiv preprint arXiv:2003.06693*, 2020.
- [35] C. Xiang, A. N. Bhagoji, V. Schwag, and P. Mittal, "{PatchGuard}: A provably robust defense against adversarial patches via small receptive fields and masking," in *30th USENIX Security Symposium (USENIX Security 21)*, 2021, pp. 2237–2254.
- [36] Z. Zhang, B. Yuan, M. McCoyd, and D. Wagner, "Clipped bagnet: Defending against sticker attacks with clipped bag-of-features," in *2020 IEEE Security and Privacy Workshops (SPW)*, pp. 55–61.
- [37] K. Sridhar, S. Dutta, R. Kaur, J. Weimer, O. Sokolsky, and I. Lee, "Towards alternative techniques for improving adversarial robustness: Analysis of adversarial training at a spectrum of perturbations," *arXiv preprint arXiv:2206.06496*, 2022.
- [38] F. Nesti, A. Biondi, and G. Buttazzo, "Detecting adversarial examples by input transformations, defense perturbations, and voting," *arXiv preprint arXiv:2101.11466*, 2021.
- [39] T. Pang, K. Xu, C. Du, N. Chen, and J. Zhu, "Improving adversarial robustness via promoting ensemble diversity," in *International Conference on Machine Learning*. PMLR, 2019, pp. 4970–4979.
- [40] J. Stallkamp, M. Schlipsing, J. Salmen, and C. Igel, "Man vs. computer: Benchmarking machine learning algorithms for traffic sign recognition," *Neural networks*, vol. 32, pp. 323–332, 2012.
- [41] J. Redmon, S. Divvala, R. Girshick, and A. Farhadi, "You only look once: Unified, real-time object detection," in *Proceedings of the IEEE conference on computer vision and pattern recognition*, 2016, pp. 779–788.
- [42] E. Yurtsever, J. Lambert, A. Carballo, and K. Takeda, "A survey of autonomous driving: Common practices and emerging technologies," *IEEE Access*, vol. 8, pp. 58 443–58 469, 2020.
- [43] A. Athalye, L. Engstrom, A. Ilyas, and K. Kwok, "Synthesizing robust adversarial examples," in *International conference on machine learning*. PMLR, 2018, pp. 284–293.
- [44] K. He, X. Zhang, S. Ren, and J. Sun, "Deep residual learning for image recognition," in *Proceedings of the IEEE conference on computer vision and pattern recognition*, 2016, pp. 770–778.